POLITECNICO DI TORINO
Repository ISTITUZIONALE

Analysis of the Shear Stresses in a Filling Line of Parenteral Products: The Role of Tubing

(Article begins on next page)

09 May 2024

Article

Analysis of the Shear Stresses in a Filling Line of Parenteral Products: The Role of Tubing

Camilla Moino [1], Bernadette Scutellà [2,*], Marco Bellini [2], Erwan Bourlès [2], Gianluca Boccardo [1] and Roberto Pisano [1]

[1] Department of Applied Science and Technology, Politecnico di Torino, 24 Corso Duca degli Abruzzi, 10129 Torino, Italy; camilla.moino@polito.it (C.M.); gianluca.boccardo@polito.it (G.B.); roberto.pisano@polito.it (R.P.)

[2] GSK, 89 Rue de l'Institut, 1330 Rixensart, Belgium; marco.x.bellini@gsk.com (M.B.); erwan.x.bourles@gsk.com (E.B.)

[*] Correspondence: bernadette.z.scutella@gsk.com

Abstract: Parenteral products appear to be sensitive to process conditions in bioprocessing steps, such as interfacial stress and shear stress. The combination of these elements is widely believed and proven to influence product stability, but the defined roles of these players in the product damage process have not yet been identified. The present work addresses a current industrial problem, by focusing on the analysis of shear stress on protein-based therapeutics flowing in tubing by means of Computational Fluid Dynamics simulations. The purpose of this article is not to pinpoint the mechanism triggering the damage of the product, but it represents the first step towards wider experimental investigations and introduces a new strategy to quantify the average shear stress. The field of scale-down approaches, used to scale the commercial process down to the laboratory level, is also explored. Since quality control is critical in the pharmaceutical realm, it is essential that the scale-down approach preserves the same stress exposure as the commercial scale, which in the present work is considered to be that resulting from shear effects. Therefore, a new approach for scaling down the commercial process is proposed, which has been compared with traditional approaches and shown to provide greater representativeness between the two scales.

Keywords: shear stress; CFD; parenteral products; filling line

1. Introduction

Fill-finish is widely considered the most critical step in the drug manufacturing process [1]. It involves a series of operations that can turn a purified drug product into the finished product, i.e., the final dosage form [2]. Fill-finish of protein-based therapeutics poses unique challenges, such as maintaining the stability and efficacy of the product throughout the process [3,4].

Proteins are polymer chains composed of amino acids [5], which are connected by free rotating bonds, and therefore, present many possible conformations, among which only a few stable ones grant the specificity of their biological functions [6]. Protein structural damage holds a great deal of biological importance; it can result in loss of the compact, native conformation, and, consequently, of its biological activity [2,7]. Several stressors have been identified and verified as protein denaturants, i.e., high temperatures, pressures [8], and mechanical forces [9,10]. In addition, structural destabilization appears to result from solid–liquid interfaces [11–14], air-liquid interfaces [15–17], and viscous stress, e.g., shear stress [18,19], which commonly occur in fill-finish manufacturing [20]. The precise role of these factors in the product damage process has not yet been universally defined and accepted, although extensively investigated [21–23]. According to some authors, shear stress can cause product damage regardless of the presence of interfaces [24,25]. Another theory holds that the damage is primarily due to the interface, possibly amplified

by high shear stress that promotes product turnover in areas in contact with the interface [22,26–28]. Furthermore, although the precise effect of exposure duration has yet to be determined, special attention should be paid to shear history. Charm and Wong [29], for example, experimentally demonstrated that catalase activity diminishes when exposure to shear increases.

Given these assumptions, it becomes paramount to precisely quantify the distribution of shear stress at a commercial scale, and control its effect during the scale-down of bioprocessing steps.

Shear stress quantifies the hydrodynamic drag force acting on a fluid [30], and is generated by its velocity gradients $\frac{du}{dx}$. Shear stress has been broadly studied in the literature [31–33]. In the case of a Newtonian fluid under laminar conditions, the Newton's law of viscosity holds [34]:

$$\sigma = \mu \, \frac{du}{dx} \tag{1}$$

where μ is the dynamic fluid viscosity. It results in shear stress having force units per unit area (Pa). Shear stress cannot easily be measured. Some velocimetry techniques can indirectly assess the wall shear stress starting from the velocity profile measurements, relying on the Doppler shift of light scattered by particles [35]. Another popular indirect device is represented by the thermal sensor, which works on the transduction of temperature to voltage [36]. Ultimately, some probes have been developed for real-time direct measurement [37], but they show high sensitivity with respect to external noise [38], which limits their use on commercial scales.

An alternative to indirect and direct measurement of the shear stress is represented by Computational Fluid Dynamics (CFD) modeling [39], which uses mathematical modeling and numerical methods to analyze and solve problems in fluid dynamics [40]. CFD is experiencing significant growth in pharmaceutical applications, as it can accelerate product and process development, facilitate optimization of existing processes, energy savings, and efficient product and process design [41].

In the biopharmaceutical field, process validation is not only a regulatory requirement, but provides an economic value; through knowledge and control of the process, batch failures are minimized [42]. In this scenario, scale-down models hold appeal in the industry; they are indispensable for process development, characterization, optimization, and validation [43]. More specifically, they allow accurate characterization of the commercial process by performing process evaluations at the laboratory level, resulting in a design space of the process that enables the control of the pharmaceutical product's Critical Quality Attributes (CQA). Such analyses are not feasible or cost-prohibitive at the commercial unit. In general, two processes are similar if they possess a geometric, kinematic, and dynamic similarity. Geometric similarity requires that linear dimensions of the original and the scaled-down system are scaled by the same ratios [34]. In turn, kinematic similarity requires geometric similarity, and the same ratio scales the velocities. Finally, dynamic similarity requires both geometric and kinematic similarity, and adds the condition that characteristic forces scale by the same ratio: specific dimensionless groups in the differential equations and boundary conditions must be the same. To provide an example, Reynolds number (*Re*) can be used to scale industrial processes; by definition, it is derived to describe the physical system in a scale-independent manner [44].

A common practice in pharmaceutical operations prescribes the replication in a laboratory unit of the worst-case scenario of the commercial line, in order to identify and employ a reasonable safety margin [45]. However, this method is time- and product-consuming, and it is not possible to make predictions in case of changes from the standard conditions of the line. A typical critical operating parameter in pipe flows is the average fluid velocity ($\bar{u}$) as a function of the pump speed.

There is still a lack of in-depth understanding of the shear stresses generated when the product goes through the line's components. This could represent the first step towards further experimental investigations.

In the present work, numerical modeling of the flow through a pipe was investigated under laminar and turbulent conditions. First, traditional scale-down and worst-case scenario approaches were tested numerically, aiming to study the result of their application to shear stress. Afterwards, a new scale-down approach was proposed in order to scale the commercial unit to the laboratory one while using the shear stress distribution as a scaling parameter. This last approach proved successful in ensuring representativeness between commercial and laboratory scales in terms of shear stress exposure.

2. Governing Equations and Theoretical Background

The continuity equation and the Navier–Stokes equation express the conservation equations of mass and momentum, and are used to estimate the pressure and velocity fields; in the case of incompressible fluids, they read as follows:

$$\frac{\partial u_i}{\partial x_i} = 0 \tag{2}$$

$$\frac{\partial u_i}{\partial t} + u_j \frac{\partial u_i}{\partial x_j} = -\frac{1}{\rho}\frac{\partial p}{\partial x_i} + \nu \frac{\partial^2 u_i}{\partial x_j^2} \tag{3}$$

where u_i is the ith component of the fluid velocity, p is the fluid pressure, and ρ and ν are its density and kinematic viscosity, respectively.

Laminar and turbulent flow regimes, which both occur in filling lines, were examined under steady-state conditions. The geometry of the flow is displayed in Figure 1, where a typical pipe flow is shown.

Figure 1. Pipe flow modeled in the present study.

For such case study, laminar flow occurs when *Re* is lower than 2100 while turbulent when it is greater than 4000. When dealing with turbulence, various modeling approaches can be used, named Reynolds Averaged Navier–Stokes (RANS), Large Eddy Simulation (LES), and Direct Numerical Simulation (DNS). The first approach resolves the mean flow, whereas the fluctuating components resulting from turbulence are modeled [46]. LES and DNS methods, on the other hand, are intrinsically more accurate, but entail a significant increase in the computational demand [47]. The RANS approach was therefore adopted under the given conditions. Within this framework, the $\kappa - \omega$ Shear Stress Transport (SST) model was used to characterize the turbulence, being a two-equation model that successfully applies in a large variety of flows [48]. It utilizes the traditional $\kappa - \omega$ model in the inner region of the boundary layer and switches to the $\kappa - \varepsilon$ model in free shear flows, thus resulting in improved capabilities [40]. The model involves the introduction of new transport equations, namely for turbulent kinetic energy (κ) and specific turbulent dissipation rate (ω). The latter is expressed as:

$$\omega = \frac{\varepsilon}{\kappa} \tag{4}$$

where ω is the turbulent dissipation rate.

The transport equations for the turbulent properties are expressed as [48,49]:

$$\frac{\partial \kappa}{\partial t} + \frac{\partial}{\partial x_i}(u_i \kappa) = P_\kappa - \beta^* \kappa \omega + \frac{\partial}{\partial x_i}\left[\left(\nu + \frac{\nu_T}{\sigma_\kappa}\right)\frac{\partial \kappa}{\partial x_i}\right] \tag{5}$$

$$\frac{\partial \omega}{\partial t} + \frac{\partial}{\partial x_i}(u_i \omega) = \alpha S^2 - \beta \omega^2 + \frac{\partial}{\partial x_i}\left[\left(\nu + \frac{\nu_T}{\sigma_\omega}\right)\frac{\partial \omega}{\partial x_i}\right] + 2(1 - F_1)\sigma_{\omega 2}\frac{1}{\omega}\frac{\partial \kappa}{\partial x_i}\frac{\partial \omega}{\partial x_i} \tag{6}$$

where F_1 is a blending function, ν_T is the turbulent kinematic viscosity, S is the invariant measure of the strain rate, and P_κ is a turbulent production term.

Each regime's relevant equations are given in two separate Sections 2.1 and 2.2.

2.1. Laminar Regime

The radial velocity profile in a circular pipe under laminar conditions is well known in the literature, and depends on the distance from the center (r):

$$u_{lam} = 2\overline{u}\left(1 - \frac{r^2}{R2}\right) \tag{7}$$

where $\overline{u}$ is the average fluid velocity, and R the tubing radius.

Combining Equations (1) and (7), the shear stress profile for a Newtonian fluid also varies linearly with respect to the distance from the center, and reaches its maximum value at the tubing wall:

$$\sigma = Q\frac{4\mu}{\pi R^4}r \tag{8}$$

where Q is the volumetric flowrate (m^3 s^{-1}).

2.2. Turbulent Regime

Under turbulent conditions, a chaotic and random state of motion develops in which pressure and velocity undergo significant fluctuations with time [50,51]. The velocity is hence decomposed into a steady mean value with a fluctuating component [40]. The mean radial velocity can be calculated as follows [52]:

$$u_{turb} = u_{max}\left(1 - \frac{r}{R}\right)^{1/n} \tag{9}$$

where n is a function of Re [53] and u_{max} is expressed as:

$$u_{max} = \overline{u}\frac{(n+1)(2n+1)}{2n^2} \tag{10}$$

Furthermore, the shear stress in such conditions is the sum of two contributions, named viscous, and turbulent shear stresses. The new turbulent term results from the Reynolds stresses and it is not straightforward to determine [54]. However, the total shear stress is still a linear function of the distance from the center and can be described as:

$$\sigma_{tot,wall} = \frac{1}{2}\rho\overline{u}^2 C_f \tag{11}$$

where C_f refers to the skin friction factor. This parameter can be computed starting from the expression of the mean velocity profile for the logarithmic-law correlation, known as Prandtl's friction law [50]. Nonetheless, the application of such an equation is not straightforward and, therefore, several approximations are available for defined Re ranges. Among those, the Blasius equation was chosen [55], being valid in the Re range of interest ($2.1 \cdot 10^3$–10^5) [34].

$$C_f = \frac{0.079}{Re^{\frac{1}{4}}} \tag{12}$$

3. Methods

3.1. Numerical Set Up

In this paper, an analysis of the shear distribution during flowing operation was conducted thanks to CFD simulations. The finite volume method-based open-source code OpenFOAM 9 (https://github.com/OpenFOAM/OpenFOAM-9 (accessed on 1 January 2022)) was used for both laminar and turbulent regimes. The simulations were carried out

on an Intel(R) Xeon(R) Gold 5118 CPU at 2.30 GHz and 128 GB of RAM. The simulations' post-processing was conducted via Python 3.8 scripts and the Paraview application.

An incompressible and Newtonian fluid was considered [56], and gravity was neglected. The peristaltic pump is commonly used in bioprocessing lines to drive the fluid across the process. It works by alternating compression and relaxation of the tubing, drawing content in and moving product away from the pump [57], thus creating a pulsating flow [58]. Since the time-averaged properties in pulsating flow are those of the steady flow under laminar and turbulent conditions [59], steady-state simulations were implemented rather than transient ones because of the more straightforward set up and lower computational cost needed.

The OpenFOAM utility blockMesh was utilized to build the tubing grid, whose length was chosen in order to ensure a fully developed flow under laminar and turbulent conditions, respectively [46]. A structured O-grid topology was chosen for the layout and smooth tubing was considered. Moreover, a traditional scale-down approach (same *Re* among the scales) and worst-case scenario approach (same $\bar{u}$) were tested numerically, named, respectively Approach 1 and Approach 2, aiming to study their effect on shear stress. The commercial internal diameter was chosen equal to 9.53 mm while the laboratory tubing was smaller, i.e., 4.76 mm, in such a way as to decrease the product consumption. These dimensions were chosen because they are those generally used industrially for pharmaceutical processes. Regarding the velocity, 0.208 m s^{-1} and 1.145 m s^{-1} were chosen for laminar and turbulent simulations, respectively.

The domains were discretized by structured grids comprised of hexahedral cells. Geometric grid expansions were used to achieve local refinement of the mesh near the boundaries, as shown in the cross-sectional tubing area of Figure 2.
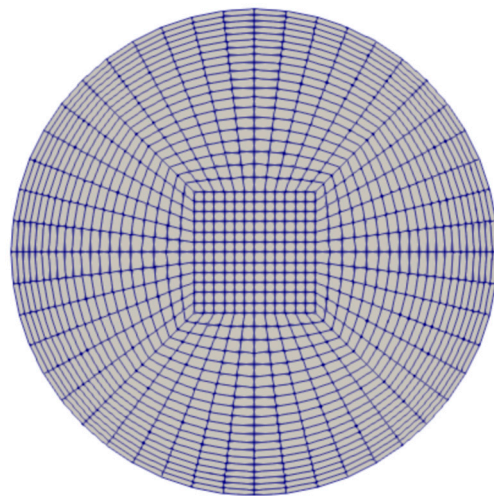

Figure 2. Typical cross-sectional mesh of the tubing.

Within the framework of the $\kappa - \omega$ SST model, y^+ insensitive wall functions were adopted. y^+ is a non-dimensional scalar quantity used to define the distance from the wall as follows: [60]

$$y^+ = \frac{y\,u^t}{\nu} \tag{13}$$

where y is the absolute distance from the wall, and u^t the friction velocity which, in turn, is derived from the wall shear stress.

Under such conditions, the boundary conditions for the turbulent properties at the wall were chosen as reported in Table 1 [49], where β is a turbulent model constant whose default value is 0.075 [49], and y_w is the distance to the first cell center normal to the wall.

Table 1. Boundary conditions at the wall, expressed in terms of OpenFOAM classes.

Turbulence Property	Boundary Condition	Estimation
κ	kLowReWallFunction	$1 \cdot 10^{-10}$
ω	omegaWallFunction	$10 \frac{6\nu}{\beta y_w^2}$
ν_T	nutLowReWallFunction	0

Defined boundary conditions were specified for the other variables. At the wall, a Dirichlet boundary condition, i.e., no-slip condition, was imposed for the velocity, while at the outlet a Neumann boundary condition, i.e., zero-gradient condition, was set. A uniform velocity was then imposed at the inlet of the tubing, since the dynamics would develop once in the fully developed region. Regarding pressure, a zero-gradient condition was chosen for the wall and the inlet of the geometry, while a uniform value (equal to 0) was used for the tubing outlet; it needs to be remembered that having employed an incompressible solver, these are values of relative pressure.

A Semi-Implicit Method for Pressure Linked Equations algorithm was used through the implementation of the simpleFoam solver, applying under-relaxation factors equal to 0.9. A Geometric Agglomerated Algebraic Multigrid (GAMG) solver was implemented for pressure, while a smooth solver coupled with the Gauss-Seidel smoother was chosen for the other variables. Regarding the convergence criterion, the threshold values for the scaled residuals were set to 10^{-6} for pressure and velocity. Along with the convergence criterion, monitoring of values of interest was performed to ensure they reached an accurate and steady solution. To this end, the analytical equations reported in Sections 2.1 and 2.2 were utilized for the comparison.

A grid independence analysis was conducted by increasing the cell number in order to find the optimal grid, resulting from a trade-off between computational cost and solution's accuracy. Such grid independence analysis was done by varying the number of cells in the blocks forming the O-grid topology and the number of cells in the z-direction. Results of the grid independence study for flow through a 9.53 mm diameter tubing in laminar and turbulent flows are shown in Figure 3, where the maximum shear stress was chosen as monitored parameter. For the sake of clarity, these values were validated by comparison to the analytical equations reported in Sections 2.1 and 2.2. Under laminar conditions, an observation can be drawn by comparing the meshes corresponding to approximately $3.3 \cdot 10^4$ and $1.1 \cdot 10^5$ cells (Figure 3a). Increasing the number of cells by an order of magnitude does not lead to a significant improvement in the accuracy of the maximum shear stress (i.e., 0.1%) and, therefore, the computationally less demanding mesh can be used for the analysis. Similar considerations can be drawn under turbulent conditions (Figure 3b).
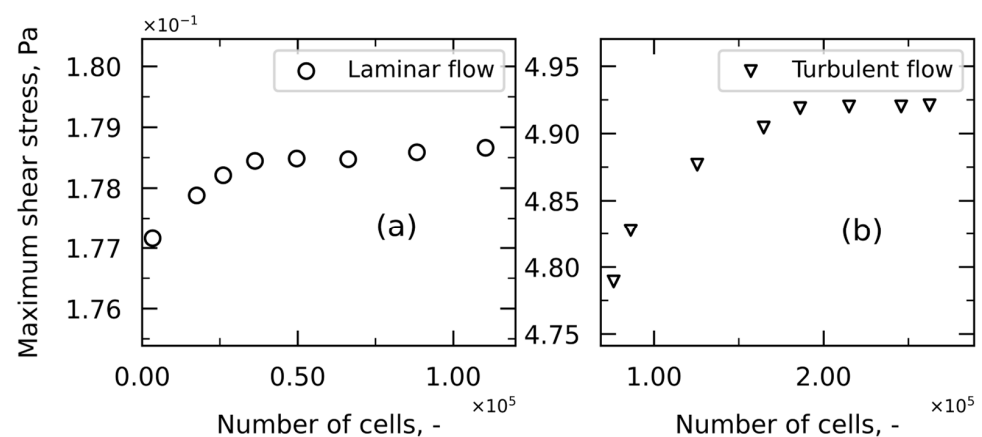
Figure 3. Grid independence analysis for the case of 9.53 mm diameter tubing under laminar (**a**) and turbulent (**b**) conditions.

Around $3.3 \cdot 10^4$ cells were used for the laminar simulations, and $1.8 \cdot 10^5$ for the turbulent simulations. Given the same fluid dynamic regime, the mesh resolution between the commercial and laboratory scales was preserved.

3.2. Shear Stress Distribution

As described in Sections 2.1 and 2.2, shear stress under both laminar and turbulent conditions varies linearly with the distance from the tubing center. This is shown in Figure 4, where the colored lines are representative of particle's trajectories uniformly released across the diameter in the tubing's fully developed region. This provides a neat visualization of the shear stress profile through the cross-sectional area.
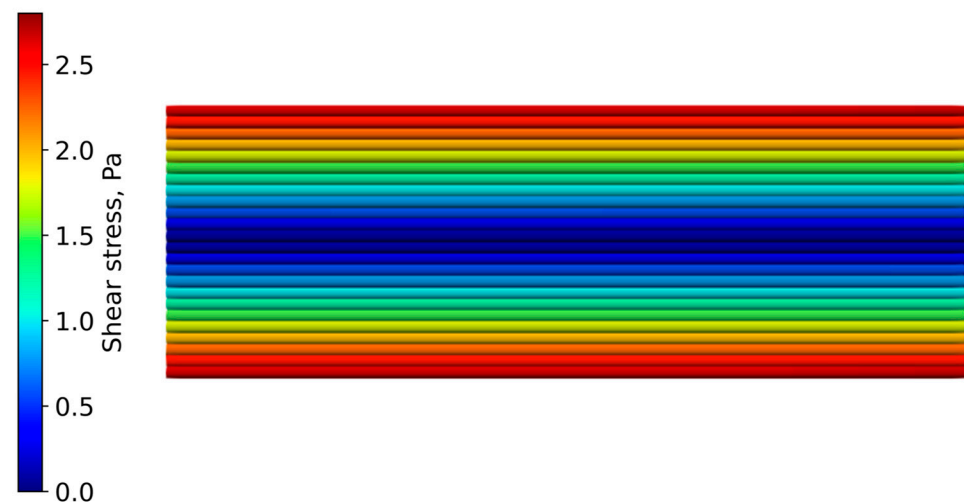

Figure 4. Shear stresses characteristic of defined particles' trajectories in the cross-section of the tubing lengthwise. Follow the color scale from blue (low shear stress) to red (high shear stress).

In bioprocessing steps, it is a common practice to refer to the maximum shear stress to characterize the hydrodynamic force acting on the product [26]. However, this phenomenon is experienced only by the fluid flowing close to the wall, as previously explained in Section 2. In addition, the fluid residence time varies through the sectional area of the tubing and reaches the lowest values at the wall, where the shear stress is the maximum. These points reveal how the effective average shear stress on the product might be a function of the volumetric flowrate that it experiences. Not surprisingly, the volumetric flowrate varies along the radial coordinate of the tubing, reaching its maximum value at the tubing center.

$$\overline{\sigma} = \frac{1}{Q_{tot}} \sum_i \sigma_i Q_i \qquad (14)$$

Therefore, Equation (14) was developed, in which the average shear stress is obtained by summing the contributions of the local shear stress weighted on the relative volumetric flowrate. For the sake of clarity, the local properties are collected by considering each cell of a tubing slice in the fully developed region. To provide an example, Figure 5 shows a typical plot for the shear stress distribution under laminar conditions; considering an arbitrary shear threshold that is 80% of the maximum value, i.e., $1.44 \cdot 10^{-1}$ Pa, Figure 5 indicates that only a small percentage of the overall product, i.e., around 12%, can experience it. Sturges' rule was applied to calculate the optimum number of bins for all the histograms hereafter presented [61].
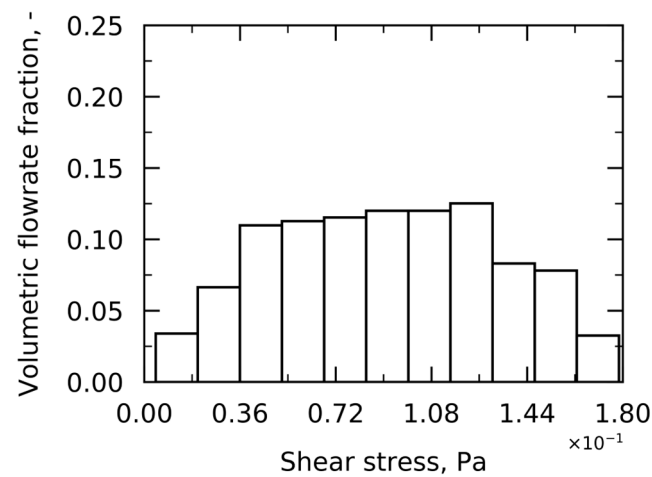
Figure 5. Shear stress distribution weighted on normalized volumetric flowrate under laminar conditions.

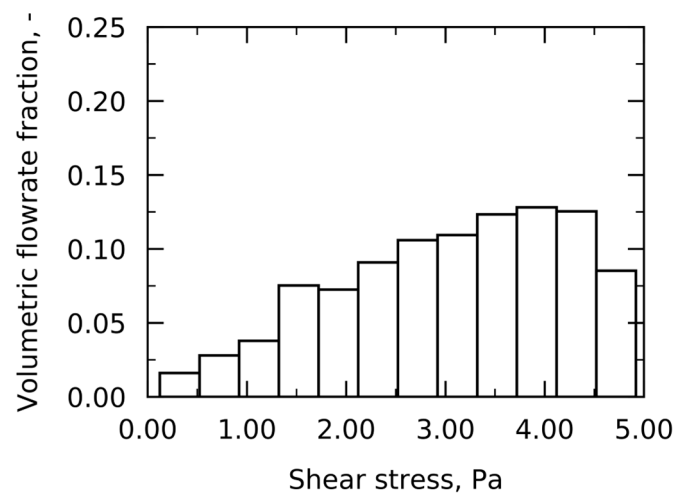Similar considerations can be drawn for Figure 6, representative of turbulent conditions.

Figure 6. Shear stress distribution weighted on normalized volumetric flowrate under turbulent conditions.

3.3. Scale-Down Approaches

Approaches 1 and 2 were numerically tested to transition from commercial to laboratory size. In addition, a new method was proposed to scale down pipe tubing using the shear stress distribution as a scaling parameter and will be further referred as Approach 3. Both laminar and turbulent regimes were investigated and are presented in two separate Sections 3.3 and 3.3.2.

3.3.1. Laminar Regime

As the shear stress distribution is the desired scale-down parameter, through manipulation of Equation (8), the inlet velocity at the laboratory level results from that used on the commercial scale as follows:

$$\overline{u}_l = \overline{u}_c \left(\frac{R_l}{R_c} \right) \tag{15}$$

where the suffixes c and l stand for commercial and laboratory, respectively.

The tubing length is calculated as to ensure the same shear stress history, i.e., same residence time:

$$\tau_l = \tau_c \tag{16}$$

$$\frac{L_l}{R_l} = \frac{L_c}{R_c} \tag{17}$$

Equation (15) presents a major benefit: while scaling to the laboratory unit, i.e., decreasing the tubing diameter, the fluid velocity is also diminished. This strategy preserves the fluid dynamics regime to be preserved among the plant scales.

3.3.2. Turbulent Regime

The wall shear stress introduced in Equation (11) was set as a scaling parameter.

$$\frac{\bar{u}_l^7}{R_l} = \frac{\bar{u}_c^7}{R_c} \tag{18}$$

By making the skin friction factor explicit, Equation (18) shows the relation which enables the wall shear stress to be constant between commercial and laboratory units.

It is worth pointing out that the skin friction factor was calculated using Blasius approximation, as presented in Section 2.2; therefore, Equation (18) is applicable only within its validity range ($2.1 \cdot 10^3$–10^5). A more widely applicable equation could be obtained by exploiting Prandtl's equation [34], where the skin friction factor is a non-linear function of the Re; however, its application is not trivial. Furthermore, when using Equation (18), care must be taken with the characteristic Re; when decreasing the tubing size at the laboratory level, the fluid velocity decreases, and so does Re. Hence, it is essential to check the *Re* number of the laboratory scale to avoid working under different fluid dynamics regimes; to avoid this concern, for example, a higher tubing diameter can be selected in the laboratory.

In a similar fashion to laminar flow, the tubing length under turbulent conditions is chosen to preserve the shear history between the scale, and thus Equation (16) is followed.

4. Results

Approaches 1 and 2 explained in Section 1 were numerically tested under laminar and turbulent conditions. Through CFD simulations, it was found that their application does not maintain the same distribution of shear stress between the scales. Figure 7 presents the results of the application of Approach 1 under both laminar and turbulent conditions. At the laboratory level, where the diameter, and hence the radius, is half that of the commercial scale, the maximum shear stress is four times higher. Therefore, the laboratory unit would not be representative of the commercial line from the perspective of the shear stress exerted on the product.
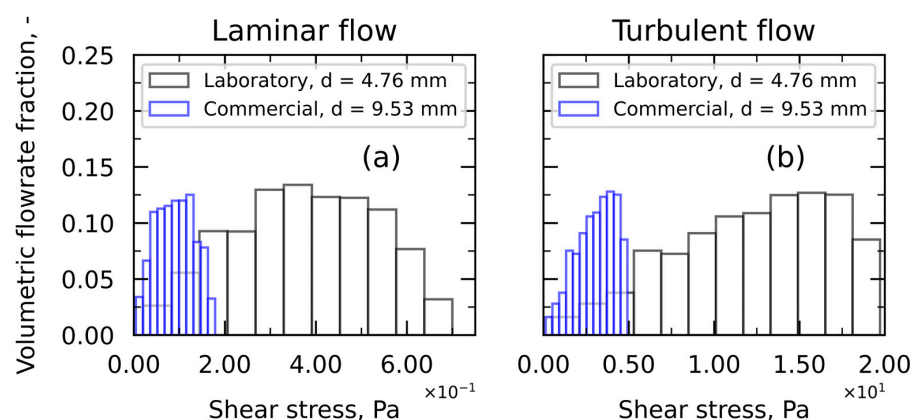

Figure 7. Shear stress distribution weighted on normalized volumetric flowrate for commercial (blue histogram) and laboratory (black histogram) unit following application of Approach 1 for laminar flow (**a**) and turbulent flow (**b**).

Similarly, the application of Approach 2 is shown in Figure 8. It results that under laminar conditions (Figure 8a), the maximum shear stress at the laboratory level would

be overestimated by a factor of 2, being the ratio between the commercial and laboratory diameter. On the other hand, under turbulent conditions (Figure 8b), the difference between the shear stress distributions does not appear to be as pronounced; however, referring to Equations (11) and (12), this disagreement increases as the diameter chosen at the laboratory scale decreases.
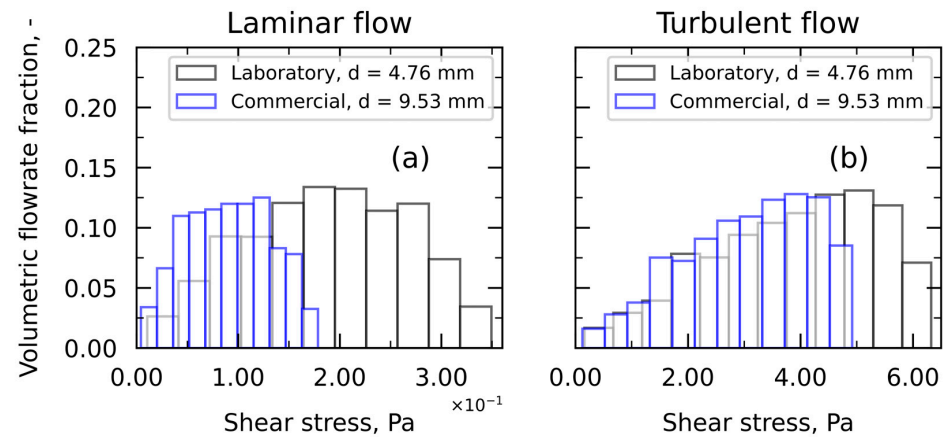

Figure 8. Shear stress distribution weighted on normalized volumetric flowrate for commercial (blue histogram) and laboratory (black histogram) unit following application of Approach 2 for laminar flow (**a**) and turbulent flow (**b**).

The application of Approach 3 (under laminar conditions) is shown in Figure 9a,b; a good consistency is observed between the shear stress distributions in the two scales.
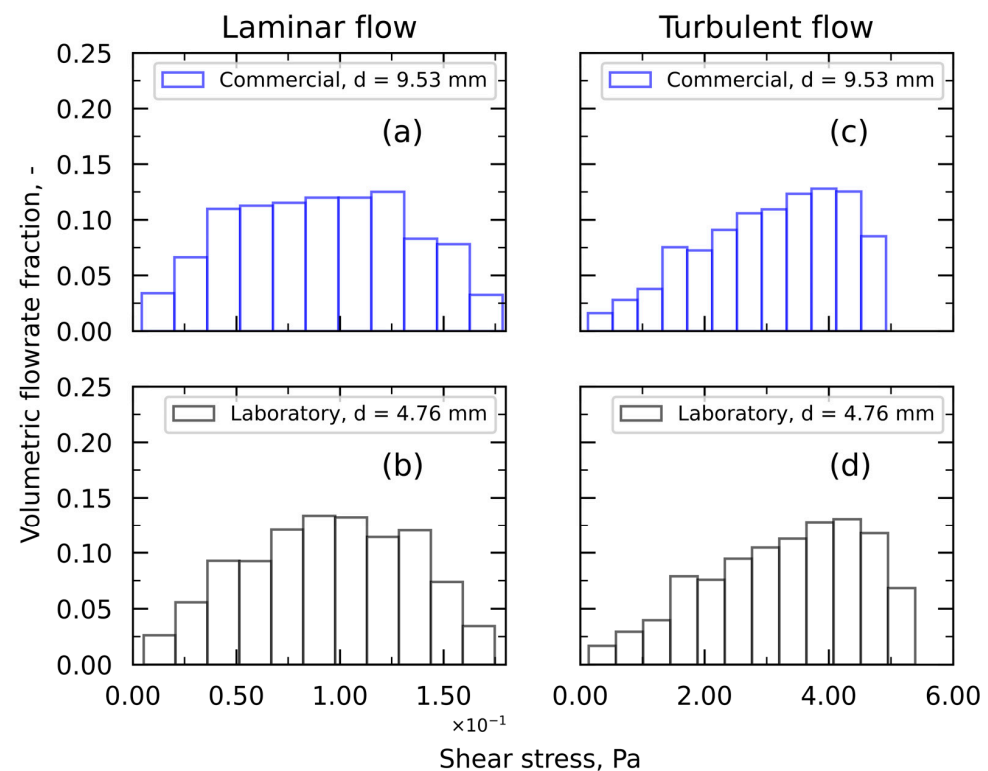

Figure 9. Shear stress distribution weighted on normalized volumetric flowrate following application of Approach 3 under laminar (**a**,**b**) and turbulent conditions (**c**,**d**) for the commercial (**a**,**c**) and laboratory scales (**b**,**d**), respectively.

Furthermore, under turbulent conditions (Figure 9c,d), the maximum shear stress is aligned between the laboratory unit and the commercial process, and so is the shear stress distribution. The slight discrepancy between the two units could be due to the fact that the average velocity at the laboratory unit is assessed using Blasius approximation and not the original equation. This choice was made to derive an equation easy to be implemented.

Table 2 summarizes the results of the tested approaches between the commercial and laboratory scales in terms of the maximum shear stresses (σ_{max}, Pa) and the effective average shear stress ($\overline{\sigma}$, Pa) calculated according to Equation (14) using the operating conditions provided in Section 3.1. Again, it can be observed that Approach 3 is the one that best ensures representativeness between commercial and laboratory units in terms of shear stress exposure.

Table 2. Comparison between the tested approaches under laminar and turbulent flow in terms of maximum shear stress (σ_{max}, Pa) and effective average shear stress ($\overline{\sigma}$, Pa) between commercial and laboratory scales.

	Approach 1		Approach 2		Approach 3	
	Commercial	Laboratory	Commercial	Laboratory	Commercial	Laboratory
laminar	$Re_l = Re_c$		$\overline{u}_l = \overline{u}_c$		$\frac{\overline{u}_l}{R_l} = \frac{\overline{u}_c}{R_c}$	
σ_{max}, Pa	0.18	0.70	0.18	0.35	0.18	0.17
$\overline{\sigma}$, Pa	0.09	0.37	0.09	0.19	0.09	0.09
turbulent	$Re_l = Re_c$		$\overline{u}_l = \overline{u}_c$		$\frac{\overline{u}_l^7}{R_l} = \frac{\overline{u}_c^7}{R_c}$	
σ_{max}, Pa	4.92	19.72	4.92	6.32	4.92	5.39
$\overline{\sigma}$, Pa	3.04	12.20	3.04	3.85	3.04	3.27

5. Conclusions

In the present work, CFD modeling was used to analyze the shear stress distribution experienced by a model product when flowing through a pipe under laminar and turbulent conditions. Numerical validation of the results was performed using the well-known analytical equations for laminar and turbulent flows. It was found that the average shear stress could be effectively calculated as a function of the volumetric flowrate that it experiences. Furthermore, a new scale-down strategy was proposed and compared with the most conventional approaches. While the traditional (Approach 1) and worst-case scenario (Approach 2) approaches were not able to ensure representativeness between commercial and laboratory scales in terms of shear stress distribution, the new approach (Approach 3) was successful. From the perspective of scale-down, maintaining the fluid dynamic regime between the commercial and laboratory scales is an essential prerequisite during the application of any scale-down approach. By applying the new scale-down method, this is ensured under laminar conditions; in turbulent flow, however, a decrease in tubing diameter can lead to a decrease in *Re*. Therefore, it is essential to carry out a careful control of the *Re* at the laboratory scale and, if necessary, choose a higher tubing diameter to remain in the turbulent regime.

This work introduces a novelty in the pharmaceutical field, where scale-down is never completed considering the process from the product's perspective. However, unlike other industrial processes, product quality control is critical; therefore, it is essential that the scale-down strategy preserves the same shear stress exposure as the commercial scale, which in the present work was considered to be that resulting from shear effects.

The following steps of this study will/could involve (i) performing experimental tests to study the effect of such shear stress distribution on product stability, (ii) wider investigating the actual shear stress distribution in pulsating flow, typical of peristaltic pumps, and (iii) extending the analysis reported in this paper to all the other components commonly present in a filling line.

Nomenclature

C_f	skin friction factor, -
F_1	blending function, -
L	tubing length, m
n	factor, -
p	pressure, Pa
P_κ	turbulent production term, $m^2\ s^{-3}$
Q	volumetric flowrate, $m^3\ s^{-1}$
r	distance from the center, m
R	tubing radius, m
Re	Reynolds number, -
S	invariant measure of the strain rate, s^{-1}
t	time, s
u	fluid velocity, $m\ s^{-1}$
$\bar{u}$	average fluid velocity, $m\ s^{-1}$
u^t	friction velocity, $m\ s^{-1}$
x	spatial coordinate, m
y	absolute distance from the wall, m
y^+	sub-layer scaled distance, -
y_w	distance to the first cell center normal to the wall, m
Greek letters	
α	turbulent model constant, -
β	turbulent model constant, -
$\beta*$	turbulent model constant, -
κ	turbulent kinetic energy, $m^2\ s^{-2}$
μ	dynamic fluid viscosity, $kg\ m^{-1}\ s^{-1}$
μ_T	turbulent eddy viscosity, $kg\ m^{-1}\ s^{-1}$
ν	kinematic viscosity, $m^2\ s^{-1}$
ν_T	turbulent kinematic viscosity, $m^2\ s^{-1}$
ρ	fluid density, $m^3\ kg^{-1}$
σ	shear stress, Pa
σ_k	turbulent model constant, -
σ_ω	turbulent model constant, -
$\sigma_{\omega 2}$	turbulent model constant, -
τ	residence time, s
ε	turbulent dissipation rate, $m^2\ s^{-3}$
ω	specific turbulent dissipation rate, s^{-1}

Subscripts

c	commercial
i	index
j	index
l	laboratory
lam	laminar
max	maximum
tot	total
turb	turbulent
wall	wall

Abbreviations

CFD	Computational Fluid Dynamics
CQA	Critical Quality Attributes
DNS	Direct Numerical Simulation
GAMG	Geometric Agglomerated Algebraic Multigrid
LES	Large Eddy Simulation
RANS	Reynolds Averaged Navier–Stokes
SST	Shear Stress Transport

References

1. Kovarcik, D.P. Critical Factors for Fill–Finish Manufacturing of Biologics. *Bioprocess Int.* **2016**. Available online: https://bioprocessintl.com/manufacturing/fill-finish/critical-factors-for-fill-finish-manufacturing-of-biologics/ (accessed on 10 March 2022).
2. Patro, S.Y.; Freund, E.; Chang, B.S. Protein formulation and fill-finish operations. *Biotechnol. Annu. Rev.* **2002**, *8*, 55–84. [CrossRef]
3. Rathore, N.; Rajan, R.S. Current perspectives on stability of protein drug products during formulation, fill and finish operations. *Biotechnol. Prog.* **2008**, *24*, 504–514. [CrossRef]
4. Das, T.K.; Sreedhara, A.; Colandene, J.D.; Chou, D.K.; Filipe, V.; Grapentin, C.; Searles, J.; Christian, T.R.; Narhi, L.O.; Jiskoot, W. Stress Factors in Protein Drug Product Manufacturing and Their Impact on Product Quality. *J. Pharm. Sci.* **2022**, *111*, 868–886. [CrossRef]
5. Buxbaum, E. *Fundamentals of Protein Structure and Function*; Springer: New York, NY, USA, 2007; ISBN 9780387263526.
6. Maddox, J. Does folding determine protein configuration? *Nature* **1994**, *370*, 13. [CrossRef]
7. Neurath, H.; Greenstein, J.P.; Putnam, F.W.; Erickson, J.O. The chemistry of protein denaturation. *Chem. Rev.* **1944**, *34*, 157–265. [CrossRef]
8. Bridgman, P.W. The Coagulation of Albumen By Pressure. *J. Biol. Chem.* **1914**, *19*, 511–512. [CrossRef]
9. Tanford, C. Protein denaturation: Part c. theoretical models for the mechanism of denaturation. *Adv. Protein Chem.* **1970**, *24*, 1–95. [CrossRef]
10. Lapidus, L.J. Protein unfolding mechanisms and their effects on folding experiments. *F1000Research* **2017**, *6*, 1723. [CrossRef]
11. Arsiccio, A.; Pisano, R. The Ice-Water Interface and Protein Stability: A Review. *J. Pharm. Sci.* **2020**, *109*, 2116–2130. [CrossRef]
12. Arsiccio, A.; McCarty, J.; Pisano, R.; Shea, J.E. Heightened Cold-Denaturation of Proteins at the Ice-Water Interface. *J. Am. Chem. Soc.* **2020**, *142*, 5722–5730. [CrossRef]
13. Arsiccio, A.; McCarty, J.; Pisano, R.; Shea, J.E. Effect of Surfactants on Surface-Induced Denaturation of Proteins: Evidence of an Orientation-Dependent Mechanism. *J. Phys. Chem. B* **2018**, *122*, 11390–11399. [CrossRef]
14. Chang, B.S.; Kendrick, B.S.; Carpenter, J.F. Surface-induced denaturation of proteins during freezing and its inhibition by surfactants. *J. Pharm. Sci.* **1996**, *85*, 1325–1330. [CrossRef]
15. Rospiccio, M.; Arsiccio, A.; Winter, G.; Pisano, R. The Role of Cyclodextrins against Interface-Induced Denaturation in Pharmaceutical Formulations: A Molecular Dynamics Approach. *Mol. Pharm.* **2021**, *18*, 2322–2333. [CrossRef]
16. D'Imprima, E.; Floris, D.; Joppe, M.; Sanchez, R.; Grininger, M.; Kuhlbrandt, W. Protein denaturation at the air-water interface and how to prevent it. *eLife* **2019**, *8*, e42747. [CrossRef]
17. Colombié, S.; Gaunand, A.; Lindet, B. Lysozyme inactivation under mechanical stirring: Effect of physical and molecular interfaces. *Enzyme Microb. Technol.* **2001**, *28*, 820–826. [CrossRef]
18. Elias, C.B.; Joshi, J.B. Role of hydrodynamic shear on activity and structure of proteins. *Adv. Biochem. Eng. Biotechnol.* **1998**, *59*, 47–71. [CrossRef]
19. Thomas, C.R.; Geer, D. Effects of shear on proteins in solution. *Biotechnol. Lett.* **2011**, *33*, 443–456. [CrossRef]
20. Li, J.; Krause, M.E.; Tu, R. *Protein Instability at Interfaces during Drug Product Development*; Springer: Cham, Switzerland, 2021; ISBN 9783030571764.
21. Murphy, R.P.; Riedel, Z.W.; Nakatani, M.A.; Salipante, P.F.; Weston, J.S.; Hudson, S.D.; Weigandt, K.M. Capillary RheoSANS: Measuring the rheology and nanostructure of complex fluids at high shear rates. *Soft Matter* **2020**, *16*, 6285–6293. [CrossRef]
22. Nesta, D.; Nanda, T.; He, J.; Haas, M.; Shpungin, S.; Rusanov, I.; Sweder, R.; Brisbane, C. Aggregation from Shear Stress and Surface Interaction: Molecule-specific or universal phenomenon? *Bioprocess. Int.* **2017**, *15*, 30–39. Available online: https://bioprocessintl.

com/analytical/pre-formulation/aggregation-shear-stress-surface-interaction-molecule-specific-universal-phenomenon/ (accessed on 16 November 2021).

23. Jaspe, J.; Hagen, S.J. Do protein molecules unfold in a simple shear flow? *Biophys. J.* **2006**, *91*, 3415–3424. [CrossRef]
24. Biddlecombe, J.G.; Craig, A.V.; Zhang, H.; Uddin, S.; Mulot, S.; Fish, B.C.; Bracewell, D.G. Determining antibody stability: Creation of solid—Liquid interfacial effects within a high shear environment. *Biotechnol. Prog.* **2007**, *23*, 1218–1222. [CrossRef] [PubMed]
25. Di Stasio, E.; De Cristofaro, R. The effect of shear stress on protein conformation: Physical forces operating on biochemical systems: The case of von Willebrand factor. *Biophys. Chem.* **2010**, *153*, 1–8. [CrossRef]
26. Bee, J.S.; Stevenson, J.L.; Mehta, B.; Svitel, J.; Pollastrini, J.; Platz, R.; Freund, E.; Carpenter, J.F.; Randolph, T.W. Response of a concentrated monoclonal antibody formulation to high shear. *Biotechnol. Bioeng.* **2009**, *103*, 936–943. [CrossRef] [PubMed]
27. Lencki, R.W.; Tecante, A.; Choplin, L. Effect of shear on the inactivation kinetics of the enzyme dextransucrase. *Biotechnol. Bioeng.* **1993**, *42*, 1061–1067. [CrossRef] [PubMed]
28. Li, J.; Krause, M.E.; Chen, X.; Cheng, Y.; Dai, W.; Hill, J.J.; Huang, M.; Jordan, S.; LaCasse, D.; Narhi, L.; et al. Interfacial Stress in the Development of Biologics: Fundamental Understanding, Current Practice, and Future Perspective. *AAPS J.* **2019**, *21*, 44. [CrossRef] [PubMed]
29. Charm, S.E.; Wong, B.L. Enzyme inactivation with shearing. *Biotechnol. Bioeng.* **1970**, *12*, 1103–1109. [CrossRef]
30. Wilkes, J.O.; Birmingham, S.G.; Kirby, B.J.; Cheng, C.-Y. *Fluid Mechanics for Chemical Engineers Second Edition with Microfluidics and CFD*, 2nd ed.; Pearson Education, Inc.: Upper Saddle River, NJ, USA, 2006; ISBN 0131482122.
31. Alsharif, A.M.; Abdellateef, A.I.; Elmaboud, Y.A.; Abdelsalam, S.I. Performance enhancement of a DC-operated micropump with electroosmosis in a hybrid nanofluid: Fractional Cattaneo heat flux problem. *Appl. Math. Mech.* **2022**, *43*, 931–944. [CrossRef]
32. Sridhar, V.; Ramesh, K.; Gnaneswara Reddy, M.; Azese, M.N.; Abdelsalam, S.I. On the entropy optimization of hemodynamic peristaltic pumping of a nanofluid with geometry effects. *Waves Random Complex Media* **2022**. [CrossRef]
33. Abdelsalam, S.I.; Mekheimer, K.S.; Zaher, A.Z. Dynamism of a hybrid Casson nanofluid with laser radiation and chemical reaction through sinusoidal channels. *Waves Random Complex Media* **2022**. [CrossRef]
34. Byron Bird, R.; Stewart, W.E.; Lightfoot, E.N. *Transport Phenomena*, 2nd ed.; John Wiley & Sons, Inc.: New York, NY, USA, 2002; ISBN 9781119130536.
35. Anderson, J. A Guide to Wall Shear Stress Measurement–#2–Indirect Measurements. 2019. Available online: https://thinkic2.com/blog/a-guide-to-wall-shear-stress-measurement-2-indirect-measurements/ (accessed on 24 February 2022).
36. Naughton, J.W.; Sheplak, M. Modern developments in shear-stress measurement. *Prog. Aerosp. Sci.* **2002**, *38*, 515–570. [CrossRef]
37. Li, W.; Pots, B.F.M.; Brown, B.; Kee, K.E.; Nesic, S. A direct measurement of wall shear stress in multiphase flow-Is it an important parameter in CO_2 corrosion of carbon steel pipelines? *Corros. Sci.* **2016**, *110*, 35–45. [CrossRef]
38. Winter, K.G. An outline of the techniques available for the measurement of skin friction in turbulent boundary layers. *Prog. Aerosp. Sci.* **1979**, *18*, 1–57. [CrossRef]
39. Katritsis, D.; Kaiktsis, L.; Chaniotis, A.; Pantos, J.; Efstathopoulos, E.P.; Marmarelis, V. Wall Shear Stress: Theoretical Considerations and Methods of Measurement. *Prog. Cardiovasc. Dis.* **2007**, *49*, 307–329. [CrossRef] [PubMed]
40. Versteeg, H.K.; Malalasekera, W. *An Introduction to Computational Fluid Dynamics*, 2nd ed.; Pearson Education, Inc.: Harlow, UK, 2007; ISBN 9780131274983.
41. Sharma, C.; Malhotra, D.; Rathore, A.S. Review of Computational fluid dynamics applications in biotechnology processes. *Biotechnol. Prog.* **2011**, *27*, 1497–1510. [CrossRef] [PubMed]
42. Rathore, A.S.; Sofer, G. *Process Validation in Manufacturing of Biopharmaceuticals*; Taylor & Francis Group, LLC.: Boca Raton, FL, USA, 2005; ISBN 9781574445169.
43. Moscariello, J. Scale-Down models: An indispensable tool to biopharmaceutical process development. *Am. Pharm. Rev.* **2016**, *19*, 48–51.
44. Al-Chi, A.; Gupta, M.R.; Stagner, W.C. *Integrated Pharmaceutics*; John Wiley & Sons, Inc.: Hoboken, NJ, USA, 2013; ISBN 9780470596920.
45. Levin, M. *Pharmaceutical Process Scale-Up*; Marcel Dekker, Inc.: New York, NY, USA, 2002; ISBN 0824706250.
46. Tu, J.; Yeoh, G.-H.; Liu, C. *Computational Fluid Dynamics*; Elsevier Ltd.: Amsterdam, The Netherlands, 2018; ISBN 9780081011270.
47. van Hooff, T.; Blocken, B.; Tominaga, Y. On the accuracy of CFD simulations of cross-ventilation flows for a generic isolated building: Comparison of RANS, LES and experiments. *Build. Environ.* **2017**, *114*, 148–165. [CrossRef]
48. Menter, F.R. Two-equation eddy-viscosity turbulence models for engineering applications. *AIAA J.* **1994**, *32*, 1598–1605. [CrossRef]
49. Guerrero, J. OpenFOAM Advanced Training. Turbulence Modeling in General CFD and OpenFOAM—Theory and Applications. 2022. Available online: http://www.wolfdynamics.com/tutorials.html?id=120 (accessed on 22 July 2022).
50. Pope, S.B. *Turbulent Flows*; Cambridge University Press: Cambridge, UK, 2000.
51. Wilcox, D.C. *Turbulence Modeling for CFD*; DCW Industries, Inc.: La Canada, CA, USA, 1994; ISBN 9283506375.
52. Stigler, J. Analytical Velocity Profile. *Eng. Mech.* **2014**, *21*, 371–379.
53. Schlichting, H. *Boundary Layer Theory*, 7th ed.; McGraw-Hill, Inc.: New York, NY, USA, 1979.
54. Kudela, H. Turbulent Flow. Available online: http://www.itcmp.pwr.wroc.pl/~znmp/dydaktyka/fundam_FM/Lecture_no3_Turbulent_flow_Modelling.pdf (accessed on 24 February 2022).

55. Trinh, K.T. On the Blasius Correlation for Friction Factors. 2010. Available online: http://arxiv.org/abs/1007.2466 (accessed on 6 April 2022).

56. Dreckmann, T.; Boeuf, J.; Ludwig, I.S.; Lümkemann, J.; Huwyler, J. Low volume aseptic filling: Impact of pump systems on shear stress. *Eur. J. Pharm. Biopharm.* **2020**, *147*, 10–18. [CrossRef]

57. Klespitz, J.; Kovács, L. Peristaltic pumps—A review on working and control possibilities. In Proceedings of the SAMI 2014—IEEE 12th International Symposium on Applied Machine Intelligence and Informatics, Herl'any, Slovakia, 23–25 January 2014; pp. 191–194.

58. Womersley, J.R. Method for the calculation of velocity, rate of flow and viscous drag in arteries when the pressure gradient is known. *J. Physiol.* **1955**, *127*, 553–563. [CrossRef] [PubMed]

59. Shemer, L.; Wygnanski, I.; Kit, E. Pulsating flow in a pipe. *J. Fluid Mech.* **1985**, *153*, 313–337. [CrossRef]

60. Liu, F. A thorough description of how wall functions Are Implemented In OpenFOAM. In *Proceedings of CFD with OpenSource Software*; Nilsson, H., Ed.; 2016; Available online: http://www.tfd.chalmers.se/~hani/kurser/OS_CFD_2016/FangqingLiu/openfoamFinal.pdf (accessed on 16 March 2022).

61. Scott, D.W. Sturges' rule. *WIRES Comput. Stat.* **2009**, *1*, 303–306. [CrossRef]